Available online at www.sciencedirect.com
ScienceDirect
International Journal of Mechanical Sciences 50 (2008) 405–421
International Journal of MECHANICAL SCIENCES
www.elsevier.com/locate/ijmecsci

Experimental based finite element simulation of cold isostatic pressing of metal powders

M. Szanto[a], W. Bier[b], N. Frage[c], S. Hartmann[b], Z. Yosibash[a,*]

[a]*Pearlstone Center for Aeronautical Engineering Studies, Department of Mechanical Engineering, Ben-Gurion University, Beer-Sheva, Israel*
[b]*Institute of Mechanics, University of Kassel, Germany*
[c]*Department of Material Engineering, Ben-Gurion University, Beer-Sheva, Israel*

Received 6 December 2006; received in revised form 10 October 2007; accepted 28 October 2007
Available online 4 November 2007

Abstract

The present work addresses the various ingredients required for reliable finite element simulations of cold isostatic pressing (CIP) of metal powders. A plastic constitutive model for finite deformation is presented and implemented into an explicit finite element (FE) code. The FE implementation is verified so that numerical errors (both temporal and spatial errors) are kept under control. Thereafter, uniaxial die compaction experiments are performed required for determining the material parameters in the constitutive model. Subsequently they are applied for the simulation of a "complex" CIP process. The experimental observations of the complex CIP process were used to validate the overall method by comparing the FE results (final dimensions and average relative density) to the experimental observations. The numerical results (final dimensions and relative density) are in good agreement with the experimental observations.

Keywords: Finite element method; Cold isostatic pressing; Metal powder

1. Introduction

Powder compaction processes are in use for manufacturing products with pre-defined shape and preferred density distribution. Determining the shape and density of a complicated product by a trial and error experimental based procedure is an expensive and time-consuming process. Hence numerical simulations are an attractive tool to reduce the amount of experiments and to provide better understanding of their results. Such simulations necessitate an appropriate constitutive model that realistically describes the material behavior and an accurate numerical method for the solution of the nonlinear system of evolution/equilibrium equations. Herein, we address a special case of powder compaction process, named "cold isostatic pressing" (CIP), for which the constitutive model of powder materials was recently proposed by Bier and Hartmann [1]. This constitutive model contains several material parameters and evolving internal variables, which should be identified for the powder of interest by simple experimental observations.

Although, numerical simulations by finite element methods (FEM) are nowadays common in the industrial manufacturing operations, CIP has been mostly based on experience and trial and error methodology. It is only recently that finite elements have been applied for the simulation of CIP processes (see Refs. [2,3] and the references therein). The main difficulties in using FE methods for CIP simulation rely on the complex finite strain constitutive models and its numerical treatment as well as the specific material parameters that have to be determined by experiments.

Constitutive models for powder compaction and determination of the material parameters on the basis of experimental data are considered by several authors [4–7]. Often experimental data from the literature are utilized, e.g. Khoei and Azami [8] used the data of an iron and copper powder mixture published by Doremus et al. [9] for the identification of the material parameters of their new cone-cap plasticity model. Chtourou et al. [10] present a detailed description of the parameter identification for their

*Corresponding author. Tel.: +972 8 6477103; fax: +972 8 6477101.
E-mail address: zohary@bgu.ac.il (Z. Yosibash).

0020-7403/$ - see front matter © 2007 Elsevier Ltd. All rights reserved.
doi:10.1016/j.ijmecsci.2007.10.004

own cap model for a steel powder. They derive their material parameters from a variety of tests consisting of resonant frequency measurements, hydrostatic compaction, triaxial compaction and uniaxial compression tests. Such detailed test data are desirable to gain maximum information on the considered material. Unfortunately such a detailed examination may not always be realized. Accordingly, the material parameters are identified based on a limited number of experimental data implying the possibility of an increasing sensitivity of the computed response.

The newly developed constitutive model for metal powder compaction presented in Ref. [1] (and slightly refined herein) is implemented into the commercial FE code Abaqus/explicit as a VUMAT user subroutine. The material parameters identified for fine grained copper powder is described in Ref. [11]. Here, we propose a slightly different model taking into account particular properties of the relative density in the limit case of infinite large hydrostatic pressure. The main goal treats the validation aspect of having a small experimental data set and its "extrapolation" to different loading processes. For the material parameters identification of the copper powder, simple die compaction experiments on cylindrical specimens, shown in Ref. [11], are conducted. A sensitivity study of the material parameter's influence on the final geometrical shape and density distribution was performed. To validate the simulation, we investigated the influence of the friction between the die and the powder on the FE results.

Thereafter, we performed experiments and FE simulations of a more "complex" geometry, a cylinder with a rigid spherical insert undergoing die compaction followed by a CIP process. To demonstrate the validity of our methods we compare the final shape and average density of the specimens with the FE results.

The paper is structured as follows: in Section 2 we present the constitutive model and its implementation in the explicit commercial FE code Abaqus/Explicit. In Section 3, we verify our FE implementation by refining the numerical discretization and monitoring the convergence of the properties of interest. We validate the constitutive model by comparing the FE results obtained by simulating the die compaction process to experimental observation. The sensitivity of the results due to the friction between the metal powder and the die is also investigated and shown to be small. In Section 4, the experimental results and FE simulations of a CIP process on "complex" cylinders with rigid spherical inserts are documented and compared to validate our methods, and we conclude by a summary and conclusions in Section 5.

2. Constitutive modeling and stress computation

Predicting the realistic response of boundary-value problems requires a constitutive model that represents the "material behavior". Because CIP and die-compaction processes involve finite strains and physically nonlinear observations, a yield function based on finite-strain elastoplasticity model proposed in Ref. [1] is applied (here a slightly modified form is proposed). The constitutive model is proven to be thermo-mechanically consistent in the sense that it fulfills the Clausius–Duhem inequality in a sufficient manner. For a self-explanatory presentation, the constitutive model is recapped in the following.

The model is based on the multiplicative decomposition of the deformation gradient, $\mathbf{F} = \mathrm{Grad}\boldsymbol{\chi}_R(\mathbf{X}, t)$, $\mathbf{F} = \mathbf{F}_e\mathbf{F}_p$, where $\mathbf{x} = \boldsymbol{\chi}_R(\mathbf{X}, t)$ defines the motion of the material point $\mathbf{X}$ at time t. $\mathbf{F}_e$ symbolizes the elastic part and $\mathbf{F}_p$ the plastic part implying an incompatible intermediate configuration. On the basis of this decomposition strain tensors can be defined, implying a dependency on purely elastic or inelastic deformations

$$\hat{\boldsymbol{\Gamma}}_e = \frac{1}{2}(\mathbf{F}_e^{\mathrm{T}}\mathbf{F}_e - \mathbf{I}),$$

$$\hat{\boldsymbol{\Gamma}}_p = \frac{1}{2}(\mathbf{I} - \mathbf{F}_p^{-\mathrm{T}}\mathbf{F}_p^{-1}),$$

$\hat{\boldsymbol{\Gamma}} = \hat{\boldsymbol{\Gamma}}_e + \hat{\boldsymbol{\Gamma}}_p = \mathbf{F}_p^{-\mathrm{T}}\mathbf{E}\mathbf{F}_p^{-1}$, with the Green strain tensor $\mathbf{E} = \frac{1}{2}(\mathbf{F}^{\mathrm{T}}\mathbf{F} - \mathbf{I})$, as well as their derivative in form of Oldroyd-derivatives relative to the inelastic intermediate configuration

$$\overset{\Delta}{\hat{\boldsymbol{\Gamma}}}_p = \hat{\mathbf{D}}_p = \dot{\hat{\boldsymbol{\Gamma}}}_p + \hat{\mathbf{L}}_p^{\mathrm{T}}\hat{\boldsymbol{\Gamma}}_p + \hat{\boldsymbol{\Gamma}}_p\hat{\mathbf{L}}_p,$$

where $\hat{\mathbf{D}}_p$ is the symmetric part of $\mathbf{L}_p = \dot{\mathbf{F}}_p\mathbf{F}_p^{-1}$. On the basis of these strain and strain-rate measures the constitutive model is motivated. First of all, the elasticity relation of Simo–Pister type is chosen, see Ref. [12],

$$\hat{\mathbf{T}} = (\Lambda \ln J_e - \mu)\mathbf{C}_e^{-1} + \mu\mathbf{I}, \tag{1}$$

where the elasticity parameters Λ and μ are Lame constants. Using the purely elastic part of the deformation, where $\hat{\mathbf{T}} = \mathbf{F}_p\tilde{\mathbf{T}}\mathbf{F}_p^{\mathrm{T}} = (\det\mathbf{F})\mathbf{F}_e^{-1}\mathbf{T}\mathbf{F}_e^{-\mathrm{T}}$ defines the stress tensor operating in the intermediate configuration, $J_e = \det\mathbf{F}_e$ the elastically volumetric deformation and the elastic right Cauchy–Green tensor $\mathbf{C}_e = \mathbf{F}_e^{\mathrm{T}}\mathbf{F}_e$. $\tilde{\mathbf{T}}$ denotes the second Piola–Kirchhoff tensor and $\mathbf{T}$ the Cauchy stress tensor (true stresses). In other words, the elasticity relation depends only on the elastic part of the deformation. The evolution of the inelastic strains is defined by an associated flow rule in form of a normality rule

$$\overset{\Delta}{\hat{\boldsymbol{\Gamma}}}_p = \lambda\frac{\partial\hat{F}}{\partial\hat{\mathbf{P}}} = \lambda\left(\frac{\partial\hat{F}}{\partial I_1}\mathbf{I} + \frac{\partial\hat{F}}{\partial J_2}\hat{\mathbf{P}}^D\right), \tag{2}$$

where $\hat{\mathbf{P}} = (\mathbf{I} + 2\hat{\boldsymbol{\Gamma}}_e)\hat{\mathbf{T}} = \hat{\mathbf{C}}_e\hat{\mathbf{T}} = \hat{\mathbf{T}}\hat{\mathbf{C}}_e$ (isotropic elastic behavior is assumed), i.e., $\hat{\mathbf{P}} = (\det\mathbf{F})\mathbf{F}_e^{\mathrm{T}}\mathbf{T}\mathbf{F}_e^{-\mathrm{T}}$, defines the Mandel stress tensor, see Ref. [13]. λ is the plastic multiplier. The proposed yield function depends on the first and second invariants $I_1 = \mathrm{tr}(\hat{\mathbf{P}})$ and $J_2 = \frac{1}{2}(\hat{\mathbf{P}}^D \cdot \hat{\mathbf{P}}^D)$

of the Mandel stress tensor as well as on two additional internal variables ξ and α in the form $\hat{F}(I_1, J_2, \xi, \alpha) = F(I_1, \sqrt{J_2}, \xi, \alpha)$. The dependency on I_1 implies pressure dependency of the yield function which reads

$$F(I_1, \sqrt{J_2}) = ck \ln\left(\frac{e^{g_1\left(I_1,\sqrt{J_2}\right)/(ck)} + e^{g_2(I_1,\sqrt{J_2})/(ck)}}{2}\right)$$

based on the log-interpolation of two simple yield functions

$$g_1(I_1, \sqrt{J_2}) = \sqrt{J_2 + \alpha(I_1 - 3\xi)^2} - k,$$

$$g_2(I_1, \sqrt{J_2}) = \sqrt{J_2 + \delta} - A_1 + A_2 e^{A_3 I_1}, \quad \delta > 0$$

using the abbreviations

$$k = \sqrt{\alpha(I_0 - 3\xi)^2},$$

$$A_1 = k(1 - \sqrt{1 - r^2})^{-I_0/((1+r)(3\xi - I_0))},$$

$$A_2 = \frac{\ln(1 - \sqrt{1 - r^2})}{(1 + r)(3\xi - I_0)}.$$

$g_1(I_1, \sqrt{J_2})$ defines an ellipsoid and $g_2(I_1, \sqrt{J_2})$ an exponential-type yield function (see Fig. 1 and Refs. [1,11] for further details). This unique, in the sense that only one closed region in stress space exists, single surface yield function is smooth and convex. In view of the flow rule (2) the derivatives read:

$$\frac{\partial \hat{F}}{\partial I_1} = \frac{\partial F}{\partial I_1} = \frac{\partial F}{\partial g_1}\frac{\partial \hat{g}_1}{\partial I_1} + \frac{\partial F}{\partial g_2}\frac{\partial \hat{g}_2}{\partial I_1},$$

$$\frac{\partial \hat{F}}{\partial J_2} = \frac{1}{2\sqrt{J_2}}\frac{\partial F}{\partial \sqrt{J_2}} = \frac{1}{2\sqrt{J_2}}\left(\frac{\partial F}{\partial g_1}\frac{\partial \hat{g}_1}{\partial \sqrt{J_2}} + \frac{\partial F}{\partial g_2}\frac{\partial \hat{g}_2}{\partial \sqrt{J_2}}\right),$$

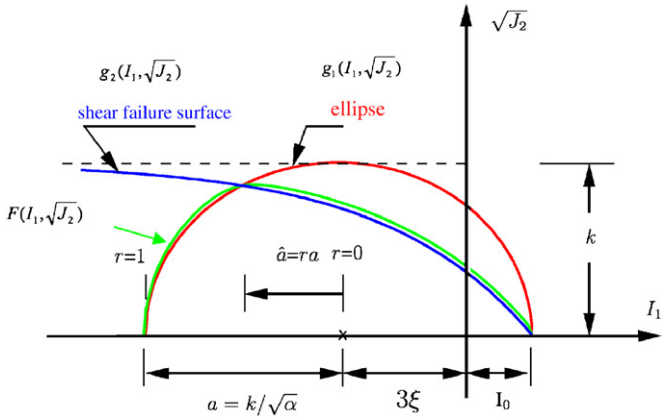

Fig. 1. Yield function ($F = 0$) in the $I_1 - \sqrt{J_2}$ plane.

$$\frac{\partial F}{\partial g_1} = \frac{e^{g_1/(ck)}}{e^{g_1/(ck)} + e^{g_2/(ck)}}, \quad \frac{\partial F}{\partial g_2} = \frac{e^{g_2/(ck)}}{e^{g_1/(ck)} + e^{g_2/(ck)}},$$

$$\frac{\partial \hat{g}_1}{\partial I_1} = \frac{\alpha(I_1 - 3\xi)}{\sqrt{J_2 + \alpha(I_1 - 3\xi)^2}}, \quad \frac{\partial \hat{g}_2}{\partial I_1} = A_2 A_3 e^{A_3 I_1},$$

$$\frac{\partial \hat{g}_1}{\partial \sqrt{J_2}} = \frac{\sqrt{J_2}}{\sqrt{J_2 + \alpha(I_1 - 3\xi)^2}}, \quad \frac{\partial \hat{g}_2}{\partial \sqrt{J_2}} = 1.$$

I_0, r and c are parameters defined in the "$I_1, \sqrt{J_2}$-plane": I_0 describes the intersection of both partial yield surfaces g_1 and g_2 with the hydrostatic axis in the tensile range and r controls the intersection point of the ellipsoid and the exponential function in the pressure region and c determines the "sharpness" of the transition. ξ and α are internal variables which evolve during the loading process.

It is guaranteed that during the yield functions evolution its convexity is satisfied. ξ evolves according to

$$\xi(r_K) = a_1 r_K + a_2 r_K^3 - \frac{a_3}{r_K - r_{K_0}} - \frac{a_3}{r_{K_0}},$$

$$r_K = \frac{1}{2}\ln(\det \mathbf{C}_p) = \ln(\det \mathbf{F}_p) \tag{3}$$

with the plastic right Cauchy–Green tensor $\mathbf{C}_p = \mathbf{F}_p^T \mathbf{F}_p$. a_1, a_2, a_3 and, r_{K_0} are material parameters and r_K is related to the relative density which can be seen for the case of rigid plasticity (no elastic domain). In this case $\det \mathbf{F} = \det \mathbf{F}_p$ holds. Accordingly, it describes the evolution of the relative density

$$\frac{\rho}{\rho_C}\det \mathbf{F} = \frac{\rho_0}{\rho_C} \to \rho_{rel} \det \mathbf{F} = \rho_{rel}^R.$$

Herein we denote by ρ_C the density of copper and by ρ_R the density in the reference configuration, where $\rho \det \mathbf{F} = \rho_R$ is exploited. The time derivative of the relative density $\rho_{rel} = \rho/\rho_C$ leads to

$$\left(\frac{d}{dt}\rho_{rel}\right)\det \mathbf{F} + \rho_{rel}\frac{d}{dt}\det \mathbf{F} = 0, \tag{4}$$

i.e., with $d/dt(\det \mathbf{F}) = (\det \mathbf{F})\mathrm{tr}\,\mathbf{D}$, $\mathbf{D} = \mathrm{sym}\,\mathbf{L}$ symbolizes the spatial strain-rate tensor, we obtain

$$\frac{d}{dt}\rho_{rel} = -\rho_{rel}\mathrm{tr}\mathbf{D}. \tag{5}$$

In the case of $\mathbf{D} = \mathbf{D}_p$

$$\frac{d}{dt}\rho_{rel} = -\rho_{rel}\mathrm{tr}\hat{\mathbf{D}}_p = -\rho_{rel}\mathrm{tr}\overset{\Delta}{\hat{\mathbf{\Gamma}}}_p = -\rho_{rel}\dot{r}_K.$$

Here, use is made of

$$\frac{d}{dt}\det \mathbf{F}_p = (\det \mathbf{F}_p)(\mathrm{tr}\hat{\mathbf{L}}_p) = (\det \mathbf{F}_p)(\mathrm{tr}\hat{\mathbf{D}}_p)$$

describing the relationship of

$$\dot{r}_K = \mathrm{tr}\hat{\mathbf{D}}_\mathrm{p} = \mathrm{tr}\overset{\Delta}{\hat{\mathbf{\Gamma}}}_\mathrm{p}.$$

The second quantity, which describes the hardening behavior of the powder material, results from the axes-ratio α of the ellipsoid where its evolution reads

$$\dot{\alpha} = \left(\frac{c_\mathrm{D}}{\alpha\chi}(\hat{\mathbf{P}} - \xi\mathbf{I}) \cdot \frac{\partial F}{\partial \hat{\mathbf{P}}} - \alpha b_\mathrm{D}\right)\dot{s},$$

i.e.,

$$\dot{\alpha} = \lambda\left(\frac{c_\mathrm{D}}{\alpha}\left((I_1 - 3\xi)\frac{\partial F}{\partial I_1} + 2J_2\frac{\partial F}{\partial J_2}\right) - b_\mathrm{D}\alpha\chi\right) \tag{6}$$

with

$$\chi = \hat{\chi}(I_1, J_2, \xi, \alpha) = \sqrt{3\left(\frac{\partial \hat{F}}{\partial I_1}\right)^2 + 2J_2\left(\frac{\partial \hat{F}}{\partial J_2}\right)^2}.$$

In this respect the rate of the plastic arc-length

$$\dot{s} = \sqrt{\overset{\Delta}{\hat{\mathbf{\Gamma}}}_\mathrm{p} \cdot \overset{\Delta}{\hat{\mathbf{\Gamma}}}_\mathrm{p}} = \lambda\chi$$

is proposed. Accordingly, the material parameters a_1, a_2, a_3 and r_{K_0} with $r_{K_0} = \ln\rho^\mathrm{R}_\mathrm{rel}$ describe the volumetric and c_D and b_D mainly the deviatoric material behavior and determine the evolution of the yield function during loading processes. These parameters are identified for regular copper powders based on the experimental results of Carnavas [14] in Ref. [1] and for irregular copper powder, based on die compaction experiments of cylindrical specimens performed by us, in Ref. [11].

Herein we use many of the material parameters as in Ref. [11] and determine others so that the modified constitutive model (3) is taken into account having the property that the relative density starts from 0.42 and cannot exceed the maximum of 1. In the following the material parameter identification is briefly recapped. For more details we refer to Refs. [1,11]. Particularly, we take over the assumptions already applied in Ref. [11] for the parameters I_0, r and c. These parameters are not identified but set a priori to reasonable values, i.e., $I_0 = 1$ MPa, $r = 0.3$ and $c = 0.01$, see Table 1, due to their geometric meaning in the yield function, see Fig. 1. c defines the interpolation factor in the yield function F controlling the closeness to the smaller of the interpolated partial yield functions. The other parameters are identified from uniaxial die-compaction experiments with intermediate unloading and reloading cycles, where a two stage procedure is proposed in Ref. [11]. In a first step a rough estimate for the parameters of the elasticity relation (1), μ and Λ, is assumed and the other parameters appearing in the evolution equation for α and $\xi(r_k)$, which describe the growth of the yield surface, are determined by a least squares fit of the simulated loading behavior to the measured loading behavior (there the measured radial and axial stresses σ_rad and σ_axial are considered). All these investigations can be done on the level of the 3-D constitutive model, because a homogeneous deformation is assumed. In the second stage, μ and Λ are determined from the unloading behavior for a fixed plastic deformation resulting in two linear equations which lead to analytical expressions for μ and Λ, for details see Ref. [11]. This procedure is done twice since the elastic parameters influence the loading process and, accordingly, the identification of the inelastic material parameters. It is shown in Ref. [11] that 2 iterations are appropriate to determine the parameters. The only difference in the current paper is the assumed relation between ξ and r_k where, instead of $\xi(r_k) = -b_1/b_2\exp(-b_2 r_k) + b_3 r_k$ assumed in Ref. [11], the new proposal (3) is applied containing the coefficients a_1, a_2, a_3 (instead of b_1, b_2, b_3). In order to simplify the identification process all parameters, except for a_1, a_2, a_3 are taken directly from Ref. [11] (namely c_D, b_D, α_0, μ and Λ) and only the parameters a_1, a_2, a_3 are determined through a least squares fit of a simulation of the loading process to the measured loading process behavior of the radial and axial stresses σ_rad and σ_axial. The entire set of parameters is compiled in Table 1.

Table 1
List of the experimentally identified material parameters

Parameter	Identified by die compaction
Λ (GPa)	5.2
μ (GPa)	8.3
I_0 (MPa)	1.0
r	0.3
c	0.01
c_D (MPa)$^{-1}$	0.0001
b_D (MPa)$^{-1}$	2.68
r_{K_0}	−0.868
a_1	24.7926
a_2	23.5836
a_3	15.9724
α_0 (initial condition)	0.558

In Ref. [11] it has also been shown that the material parameters μ and Λ should be density dependent (in this respect see also the discussions in Refs. [15,16]). Nevertheless the influence of keeping these parameters as constants was found to be of minor importance as one may see at the elastic loading and unloading curves: the estimated constant parameters produce predictions that lie in between the experimental data (see Fig. 15 in Ref. [11]). In a future investigation a thermomechanical consistent model, which is also capable to consider density dependent μ and Λ will be derived.

In Table 1 the material parameters used in subsequent analyses are summarized.

Implementation of the constitutive model in an explicit FE code: Since the complicated loading process in real

applications imply the computation of the underlying initial boundary-value problem, use is made of Abaqus/explicit. To this end, the constitutive model has to be incorporated into the FE program using the VUMAT-interface. Explicit finite elements, see, for example, Belytschko et al. [17], are based on the discretized equation of motion

$$\mathbf{M}\mathbf{a}(t) = \bar{\mathbf{p}}(t) - \mathbf{g}(t, \mathbf{u}, \mathbf{q}), \tag{7}$$

with the mass matrix $\mathbf{M}$, the externally prescribed force vector $\bar{\mathbf{p}}(t)$ and the internal force vector $\mathbf{g}(t, \mathbf{u}, \mathbf{q})$ which contains the current stress state. $\mathbf{a}$ and $\mathbf{u}$ are the acceleration and the displacement vector respectively and $\mathbf{q}$ contains all internal variables of all Gauss-points of the structure. Eq. (7) has to be fulfilled at each time t_n:

$$\mathbf{M}\mathbf{a}_n = \bar{\mathbf{p}}(t_n) - \mathbf{g}(t_n, \mathbf{u}_n, \mathbf{q}_n). \tag{8}$$

Applying this relation requires the internal force vector $\mathbf{g}(t_{n+1}, \mathbf{u}_{n+1}, \mathbf{q}_{n+1})$ for the next step, i.e., the stresses at the time t_{n+1}, which depend on the constitutive model, on the displacements (deformation gradient) and the internal variables, defined by a case distinction (elasticity or plasticity in dependence of the loading condition). In the purely elastic case only Eq. (8) has to be computed. In the inelastic case (at these Gauss-points where plastic loading occurs), the second order system of differential algebraic equations (DAE)

$$\mathbf{M}\mathbf{a}_n = \bar{\mathbf{p}}(t_n) - \mathbf{g}(t_n, \mathbf{u}_n, \mathbf{q}_n), \tag{9}$$

$$\dot{\mathbf{q}} = \mathbf{r}(t_n, \mathbf{u}_n, \mathbf{q}_n, \boldsymbol{\lambda}_n), \tag{10}$$

$$\mathbf{f}(t_n, \mathbf{u}_n, \mathbf{q}_n) = \mathbf{0} \tag{11}$$

has to be solved. This is solved in the context of explicit formulation by a partitioned integration method, i.e., for different parts of the coupled system different integrators are applied. A central difference method is applied to discretize (9) leading to the displacements

$$\mathbf{u}_{n+1} = \mathbf{u}_n + \Delta t_{n+1}\left(\mathbf{v}_{n-\frac{1}{2}} + \frac{\Delta t_{n+1} - \Delta t_n}{2}\mathbf{a}_n\right) \tag{12}$$

with

$$\mathbf{v}_{n-\frac{1}{2}} = \frac{1}{\Delta t_n}(\mathbf{u}_n - \mathbf{u}_{n-1}) \quad \text{and} \quad \Delta t_{n+1} = t_{n+1} - t_n,$$
$$\Delta t_n = t_n - t_{n-1}.$$

The first order DAE-system (10) and (11) is usually solved by a Backward–Euler method where the computed displacements (12) are used

$$\mathbf{q}_{n+1} = \mathbf{q}_n + \Delta t_{n+1}\mathbf{r}(t_{n+1}, \mathbf{u}_{n+1}, \mathbf{q}_{n+1}, \boldsymbol{\lambda}_{n+1}),$$

$$\mathbf{f}(t_{n+1}, \mathbf{u}_{n+1}, \mathbf{q}_{n+1}) = \mathbf{0}.$$

$\mathbf{f}$ are all yield conditions currently active and $\boldsymbol{\lambda}_{n+1}$ the plastic multipliers concerned. In other words an explicit method is combined with an implicit method.

In respect to the numerical treatment of the constitutive model, the evolution equations (2)–(4) and the stresses (1) are expressed by quantities relative to the reference configuration, $\tilde{\mathbf{T}} = \mathbf{h}(\mathbf{C}, \mathbf{C}_p)$, and integrated by means of an elastic predictor—plastic corrector scheme on the basis of Backward–Euler method, see Hartmann and Bier [18] for a detailed explanation. There, a fully implicit solution scheme and time-adaptive procedures are investigated.

3. Die-compaction: verification and validation of the FE code

The constitutive model has been implemented in the explicit commercial code Abaqus/Explicit. Herein we present the verification of the FE implementation and its validation by comparison to the die compaction experiments. In the following section, the validation of the code under a 3-D setting is performed by analyzing a CIP process and comparing the results to experimental observations.

3.1. Verification of FE simulations

The material parameters in Table 1, identified by die-compaction experiments, were used in a FE analysis that simulates the experiments for verification and validation purposes. A 2-D axisymmetric domain is considered, where only one forth of the geometry is modeled. Following the experimental setup [11] the computational domain is shown in Fig. 2. The specimen is 14 mm in diameter and 17.3 mm in height. The die and punches are made of 4340 steel, with Young's modulus $E = 200$ GPa, Poisson ratio $\nu = 0.3$ and yield strength of $\sigma_Y = 1300$ MPa, guaranteeing the elastic behavior. On the top of the upper punch, a pressure of 500 MPa is applied (loading), which is removed during the unloading process.

A systematic space enrichment is performed by increasing the mesh densities of 2×1, 8×6 (48 elements), 16×12 (192 elements). In these analyses quadrilateral axisymmetric

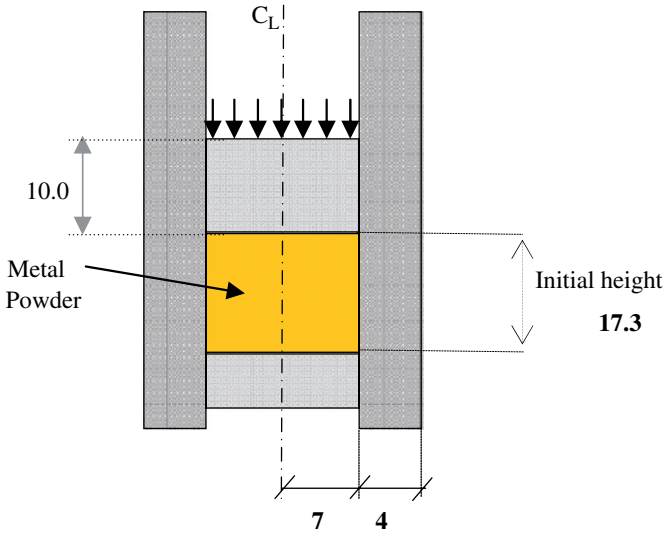

Fig. 2. Geometry of the die-compaction model.

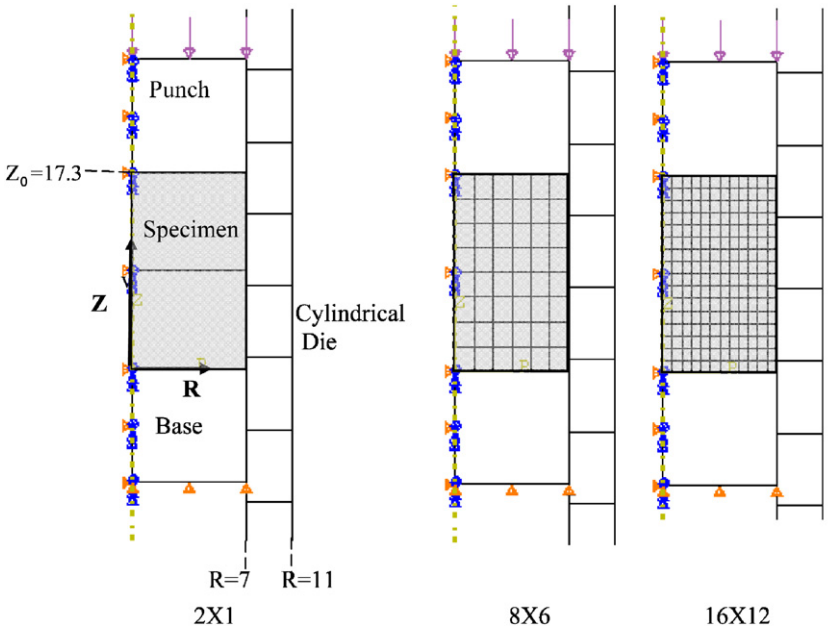

Fig. 3. Discretization (different mesh densities) of the die compaction analysis.

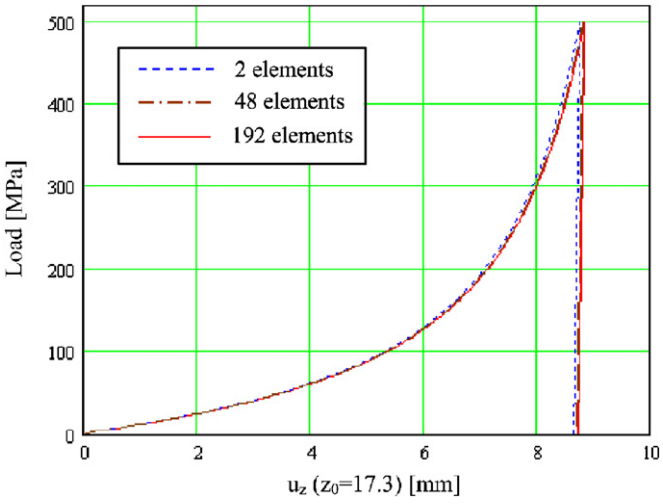

Fig. 4. Die compaction: axial displacement versus the load using frictionless contact for different mesh densities.

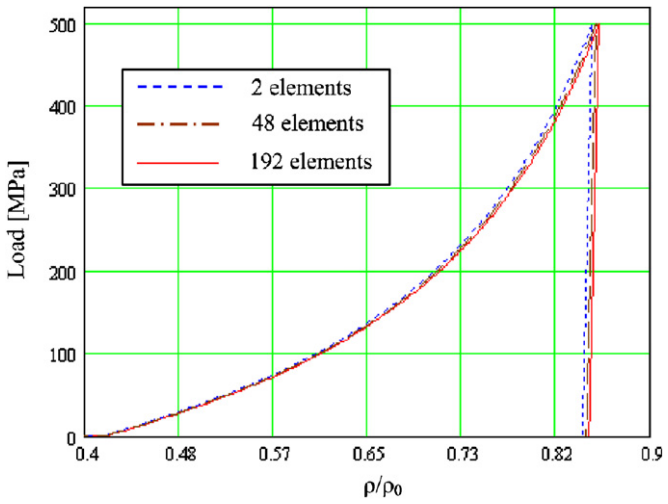

Fig. 5. Die compaction: average relative density versus the load using frictionless contact for different mesh densities.

reduced integration elements are used. The upper and lower punches are represented by a single element and the cylindrical die consists of 3 elements in the vicinity of the specimen, see Fig. 3.

Contact surfaces with optional friction defined between the punches, cylindrical die and the specimen, whereas in the present subsection frictionless assumption is used.

For this analysis the relative density ρ_{rel} is necessary, which is determined by the determinant of the deformation gradient at the Gauss-point (here, the one-point integration is exploited), see Eq. (4). The initial relative density, as determined by experimental results in Ref. [11], is $\rho_{\text{rel}}^{\text{R}} = 0.42$.

The computational results of the axial displacement at the top of the specimen ($z_0 = 17.3$) and the relative density versus the load, using frictionless contact for the different mesh densities of the specimen are plotted in Figs. 4 and 5, respectively. The displacement under the maximum and after the release of the load for the different mesh densities is reported in Table 2.

The relative density for the frictionless boundary conditions should be identical over the specimen. However, because of the numerical explicit scheme, a small deviation of less then 0.2% exists, hence the relative density, plotted in the different figures is the average value over the entire specimen.

3.2. Die compaction: experimental vs. computational validation

The die-compaction experiments (with a load of 500 MPa) and the material parameter identification based

Table 2
FE results for the die-compaction simulation (for frictionless contact)

DOF (number of elements)	Step size during unloading	Step size during loading	Maximum displacement U_z ($z_0 = 17.3$) at unloading (mm)	Maximum displacement U_z ($z_0 = 17.3$) at loading (mm)
9 (2)	1×10^{-6}	1×10^{-6}	8.834270	8.724890
117 (48)	1×10^{-6}	1×10^{-6}	8.807767	8.698715
425 (192)	1×10^{-7}	1×10^{-8}	8.754762	8.646366

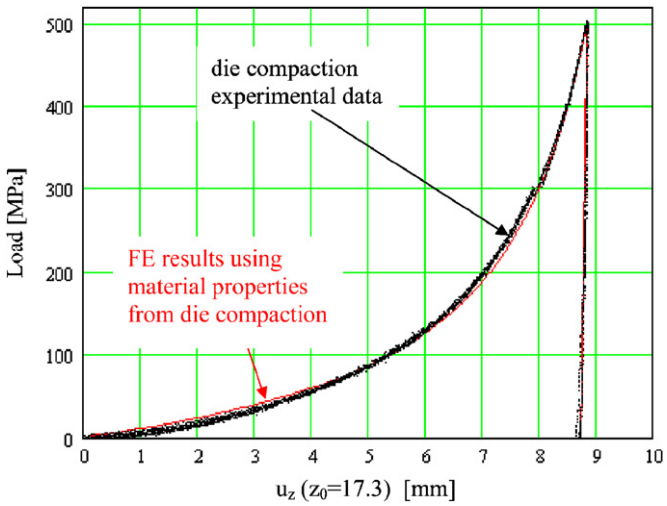

Fig. 6. Experimental and FE axial displacement on the top vs. applied load.

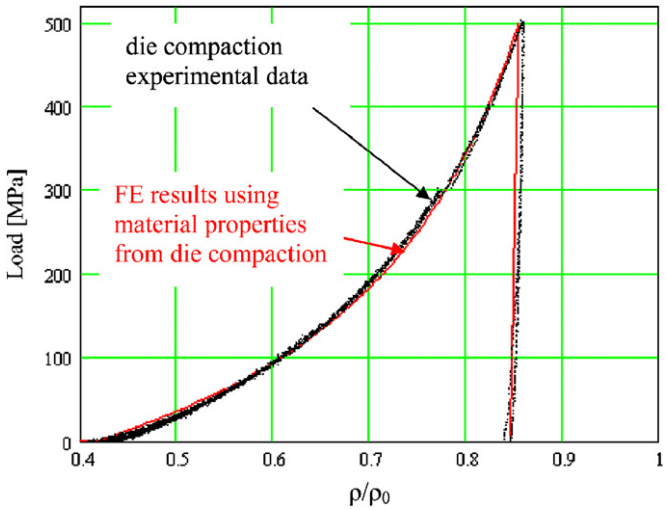

Fig. 7. Experimental and FE average relative density vs. applied load.

on their results are reported in Ref. [11]. In order to compare the observations of the experiments (loading and unloading) with the FE solutions we used the 48 elements mesh described in the previous section. The FE axial displacement (at $z_0 = 17.3$) and averaged relative density versus the applied load are plotted in Figs. 6 and 7, respectively (peak values reported in Tables 3 and 4). The

Table 3
Maximum relative density in die compaction—FE and experimental results

	Relative density ρ/ρ_0	
	FE results with material parameters identified by die compaction exp.	Die compaction experimental data
Loading	0.854	0.858
Unloading	0.845	0.845

Table 4
Maximum axial displacements [mm] in die compaction—FE and experimental results

	Axial displacement u_z ($z_0 = 17.3$)	
	FE results with material parameters identified by die compaction exp.	Die compaction experimental data
Loading	8.834	8.835
Unloading	8.794	8.700

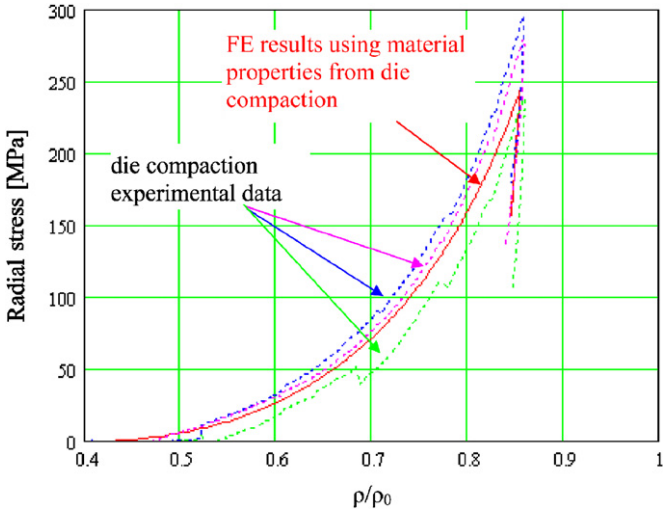

Fig. 8. Radial stress vs. average relative density of the 3 different experimental data.

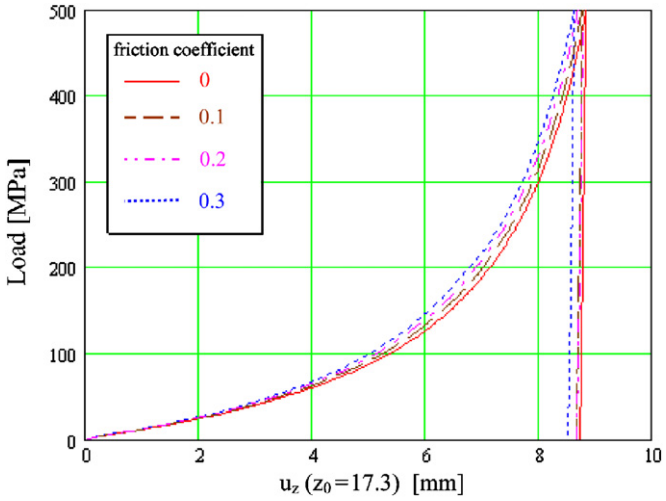

Fig. 9. Die compaction FE analysis: axial displacement vs. load for different friction coefficients.

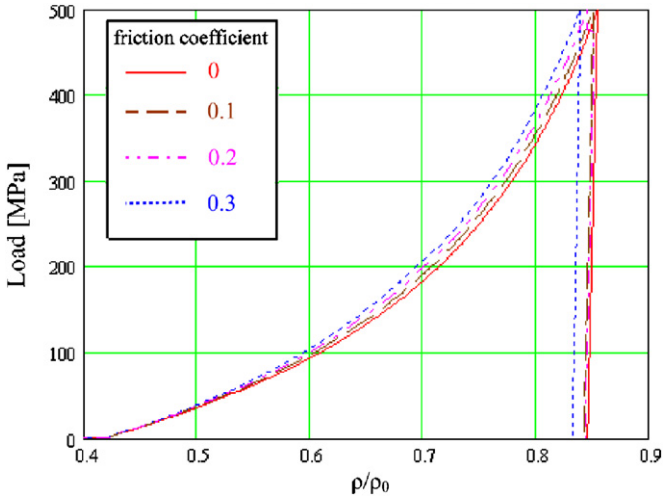

Fig. 10. Die compaction FE analysis: average relative density vs. load for different friction coefficients.

FE results are compared to die-compaction measurements available from three different experiments.

The radial stress applied inside the die is computed in Ref. [11] based on the measured radial displacement outside the die at a fixed position, under the assumption of linear elastic response of the die. The measured radial displacements are in a scale of μm. These small values may result in some loss in accuracy. Hence, the values of radial stress have relatively large deviation between the data of the 3 experiments as shown in Fig. 8.

3.3. Die compaction: on the influence of friction

The purpose of the die compaction experiment was to identify the material parameters by obtaining a state of homogeneous deformation. However, due to the inevitable friction between the die and the metal powder one cannot obtain a pure state of homogeneous deformation. Therefore, it is important to identify the effect of the friction on the parameter identification. Hence, a parametric computation for friction coefficients of 0, 0.1, 0.2, 0.3, between the metal powder and the dies was performed. Using the material parameters obtained from die-compaction experiment with the assumption of frictionless contact we performed FE analyses of the die-compaction experiment using the 48 elements mesh. The axial displacement versus the load, and the average relative density for different friction coefficients is plotted in Figs. 9 and 10, respectively. The relative density distributions shown in Fig. 11 confirm the anticipated increase in the relative density distribution with the increase of friction coefficient, and indicate higher values at the top close to the upper punch. Hence, values of the relative densities plotted in the following figures, are average values. The results of the averaged relative densities indicate only a small dependence of the process on the friction between the specimen and the die. The displacement, relative density and stresses at maximum load and after unloading are reported in Tables 5 and 6.

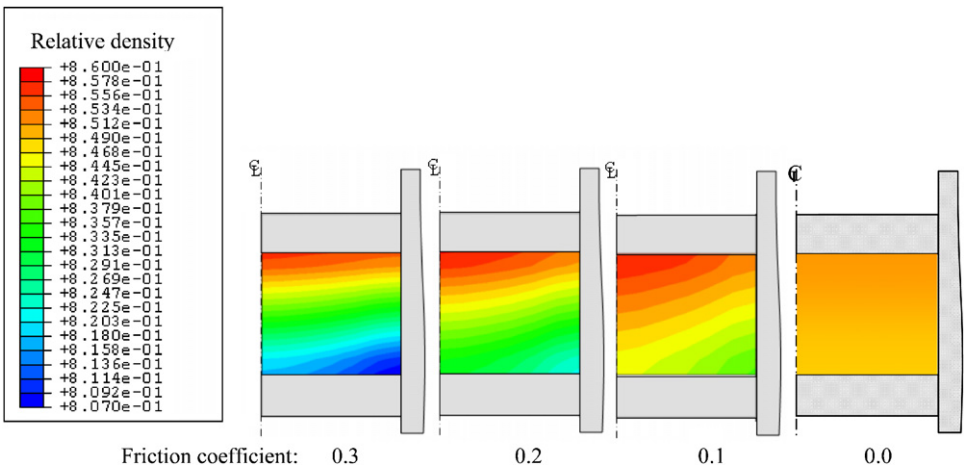

Fig. 11. Die compaction FE analysis: effect of the friction coefficient on the relative density distribution in die compaction.

Table 5
Computational results of the stresses, for different friction coefficients

Friction coefficient	Maximum axial stress (MPa)	Maximum axial stress at unloading (MPa)	Maximum radial stress (MPa)	Maximum radial stress at unloading (MPa)
0	500	0	242.523	156.127
0.1	500	22.5501	248.022	171.056
0.2	500	23.6828	249.211	178.855
0.3	500	27.9833	250.828	185.435

Table 6
Density and displacements, for different friction coefficients

Friction coefficient	Maximum relative density ρ/ρ_0	Relative density ρ/ρ_0 at unloading	Maximum axial displacement u_z ($z_0 = 17.3$) (mm)	Axial displacement at unloading u_z ($z_0 = 17.3$) (mm)	Maximum radial displacement u_r ($r_0 = 7.0$) (mm)
0	0.854269	0.845503	8.83427	8.79390	$13.58404 \cdot 10^{-3}$
0.1	0.850413	0.842918	8.76558	8.75319	$13.35707 \cdot 10^{-3}$
0.2	0.845201	0.840304	8.69091	8.68818	$12.93288 \cdot 10^{-3}$
0.3	0.838787	0.831523	8.61834	8.51043	$12.61476 \cdot 10^{-3}$

3.4. A preliminary sensitivity study

To obtain a "feeling" on the influence of a small change in material parameters on the final dimension and density following a die compaction analysis, we performed two rough sensitivity studies. For this purpose we performed FE analysis of die compaction using the 48 elements mesh. In the first sensitivity study we varied mutually the parameters a_1, a_2, a_3, that define the evolution of the yield surface, by $\pm 10\%$ (equivalent to variation of $\pm 10\%$ in ξ). The resulting FE axial displacements and the relative densities as a function of the load are plotted in Fig. 12. One may notice that there is a change in the response at the same order of magnitude (about 10%) because of the change of material parameters, i.e., the influence is proportional.

In the second sensitivity analysis the variation in the parameters a_1, a_2, a_3, and rk_0, that define the evolution of the yield surface, were tested separately. Each parameter, x_i was varied by a small amount of Δx_i, and the numerical gradient was computed as follows:

$$rel\_grad(x_i)_{\rho/\rho_0} = x_i \cdot \frac{\rho/\rho_0(x_i + \Delta x_i) - \rho/\rho_0(x_i)}{\Delta x_i},$$
$$rel\_grad(x_i)_u = x_i \cdot \frac{u(x_i + \Delta x_i) - u(x_i)}{\Delta x_i}. \quad (13)$$

The resulting FE variation in axial displacements and the relative densities as a function of the load are plotted in Figs. 13(a) and (b). These results indicate that variation in rk_0 has the highest impact on the results, whereas the variation in a_2 has the least influence on the results.

When examining the spring-back displacement after unloading, one notices it is considerably smaller than the total displacement. This is because the unloading is in the elastic range. Thus the governing parameters are the "Lame constants" μ and Λ. These parameters are assumed to be constant during the entire die compaction process (see Ref. [11]). In other words the value of the spring-back displacement can be controlled by these parameters.

4. CIP of a complex specimen

In order to validate our constitutive model and FE implementation a more complex geometry is considered, undergoing a die-compaction followed by a CIP process. A cylindrical sample made of copper powder (same as used in Section 3) with a rigid sphere insert is considered as shown in Fig. 14(a). The specimen is loaded in two stages. At first, from a relative density of approximately 0.42 to an average relative density of about 0.53, by die compaction (axial load), compressing it to 52 MPa. In the second stage, the specimen is removed from the die and placed in a pressure chamber, where it is subjected to a uniform isostatic pressure (CIP) of 300 MPa. The specimen dimensions, after die compaction, are shown in Fig. 14(b).

In the experimental data of compaction with a spherical insert the initial height of the loose powder in the die was not measured, i.e., in order to use the material properties determined in Section 3, we assume an initial relative density of 0.42, which corresponds to a height of 29.0 mm. We obtain after the die compaction process an average density of 0.53 at a height of 23.5 mm, identical to the experimental value. After the unloading of the die, the specimen was placed in the pressure chamber and loaded by an isostatic pressure to 300 MPa, after which the

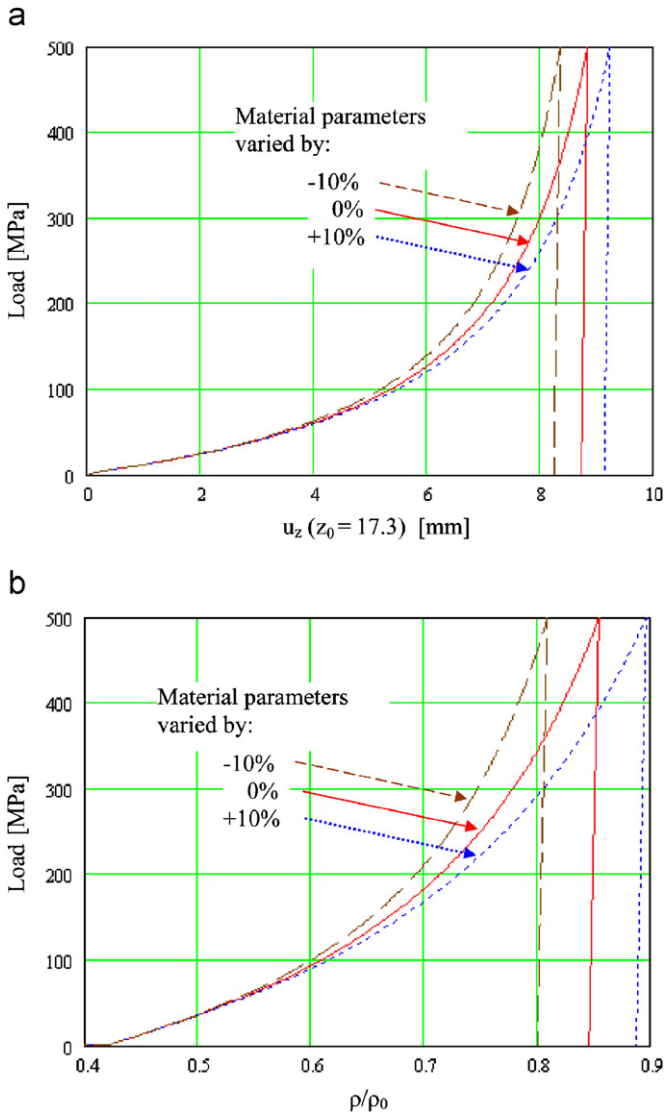

Fig. 12. Die compaction FE analysis: (a) influence of material parameters on axial displacement vs. load response, (b) influence of material parameters on average relative density vs. load response.

pressure was released and the specimen removed from the chamber. The final shape of the specimen is shown in Fig. 15.

In view of the radial and axial symmetry, only one fourth of the domain was modeled as in the previous section. The available axisymmetric elements in the software product Abaqus/Explicit allow only bilinear quadrilaterals (4-nodes) with reduced integration or quadratic triangular elements with reduced integration. We have used both for the numerical experiments. Four different meshes were considered: two quadrilateral meshes, one with a coarse and another with a fine mesh, and two triangular meshes, one with 3-noded (linear) and second with 6-noded (quadratic) elements. The four meshes are shown in Figs. 16 and 17. The inserted sphere is made of a stainless steel which is simulated by a rigid inclusion (Young modulus of the sphere is considerably higher compared to the copper powder). Furthermore, another simplification is introduced by clamping the circular boundary of the powder which imply full contact between the powder and the circular sphere. The die and punch are made of high grade steel thus are modeled as rigid bodies which are in frictionless contact with the metal powder (allow to slide).

Following the actual experimental procedure, the FE analysis was divided in four stages:

1. Die compaction from a height of 29 to 23.5 mm.
2. Release of the punch followed by a release of the die by their motion away from the compacted specimen.
3. CIP of the specimen, by applying a uniform pressure of 300 MPa on outer boundary.
4. Decrease of the pressure to zero (unloading).

For the explicit scheme we chose a very small time step of $\Delta t = 10^{-7}$ to assure small temporal integration errors. The entire process was divided into 16×10^7 time-steps as follows: 5×10^7 time-steps for the die compaction, 2×10^7 for the release of the die, 7×10^7 for the CIP process and 2×10^7 for the pressure release (unloading).

Fig. 18 presents the relative density distribution after die compaction for the four different meshes used in our analysis. Following the die compaction and the release of the specimen from the dies, the CIP process was modeled by applying a uniformly distributed pressure of 300 MPa over the outer surface following by unloading where the pressure is gradually reduced to zero. The relative density distribution at the end of the process, (i.e., after the CIP and unloading) plotted in Fig. 19.

We also summarize the maximum and minimum height and diameters as obtained from the FE analyses compared to the experimental observations in Table 7 (see definitions of $H_{\max}$, $H_{\min}$, $D_{\max}$, $D_{\min}$ in Fig. 15). The reported experimental data are the average of 5 specimens tested (detailed information on the experimental measurements is provided in Appendix A). Because it was not possible to measure the relative density pointwise in the experimental specimens (the obtained measurement error was too large), we computed from the FE simulation the average relative density to compare it to the one obtained in experiments—this comparison is shown also in Table 7.

The averaged specimen's density was measured in the experiments by the "water displacement method" also known as the "Archimedes method". The samples were infiltrated with distilled water in vacuum (density of distilled water is taken as $1\,\mathrm{g/cm^3}$ at room temperature). Denoting the three *measured masses* of a sample by: W_D mass of dry sample (known from the powder's mass prior to the experiment), W_W its mass with water and W_S mass of specimen immersed in water, and denoting by R the spherical insert radius with its mass equal to $m_{insert} = \rho_{insert} * \frac{4}{3}\pi R^3$ we computed the following

quantities:

$$W_{D1} = W_D - m_{insert},$$
$$W_{W1} = W_W - m_{insert},$$
$$W_{S1} = W_S - (m_{insert} - V_{insert} \times \rho_{water}).$$

Then we computed the average density of the copper specimen by

$$V_{OpenPorosity} = (W_{W1} - W_{D1})/\rho_{water},$$

$$V_{PM} = (W_{D1} - W_{S1})/\rho_{water} + V_{OpenPorosity} = (W_{W1} - W_{S1})/\rho_{water},$$

$$\rho_{PM} = \frac{W_{PM}}{V_{PM}} = \frac{W_{D1}}{(W_{W1} - W_{S1})/\rho_{water}}.$$

One may also noticed that the deformed shape of the specimen after the CIP process, as shown in Fig. 19, results in a non-flat surfaces at the top (and bottom) of the specimen and barrel at the circumference, as also observed in the experiments.

The obtained results are in very close agreement with the experimental observations.

It is also evident that the numerical errors are small since the results of the various models are very close.

Notes on the time step size: The FE solution is obtained by the combination of an explicit scheme for the momentum equation and an implicit scheme for the

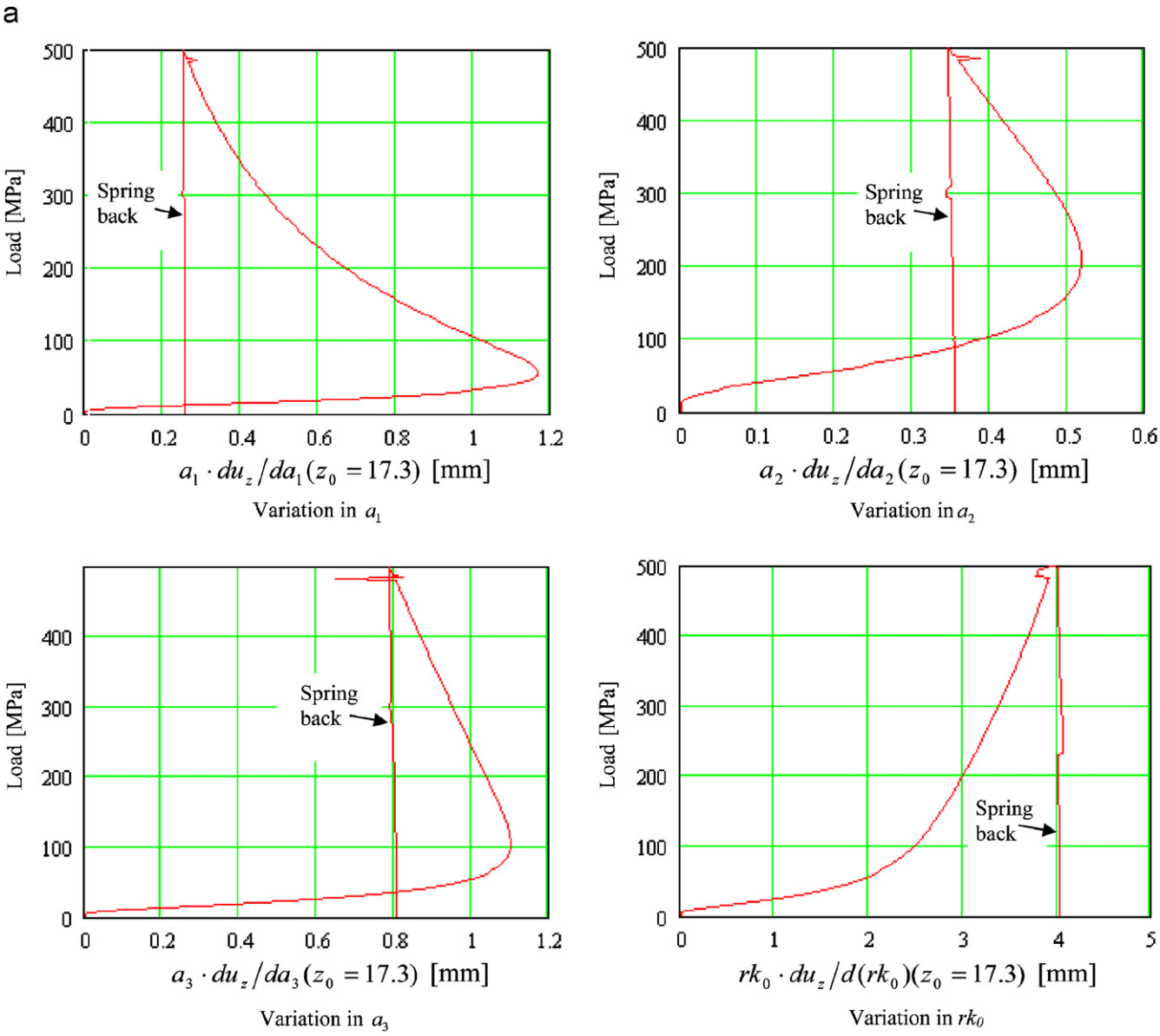

Fig. 13a. Die compaction FE analysis: influence of material parameters on axial displacement vs. load response.

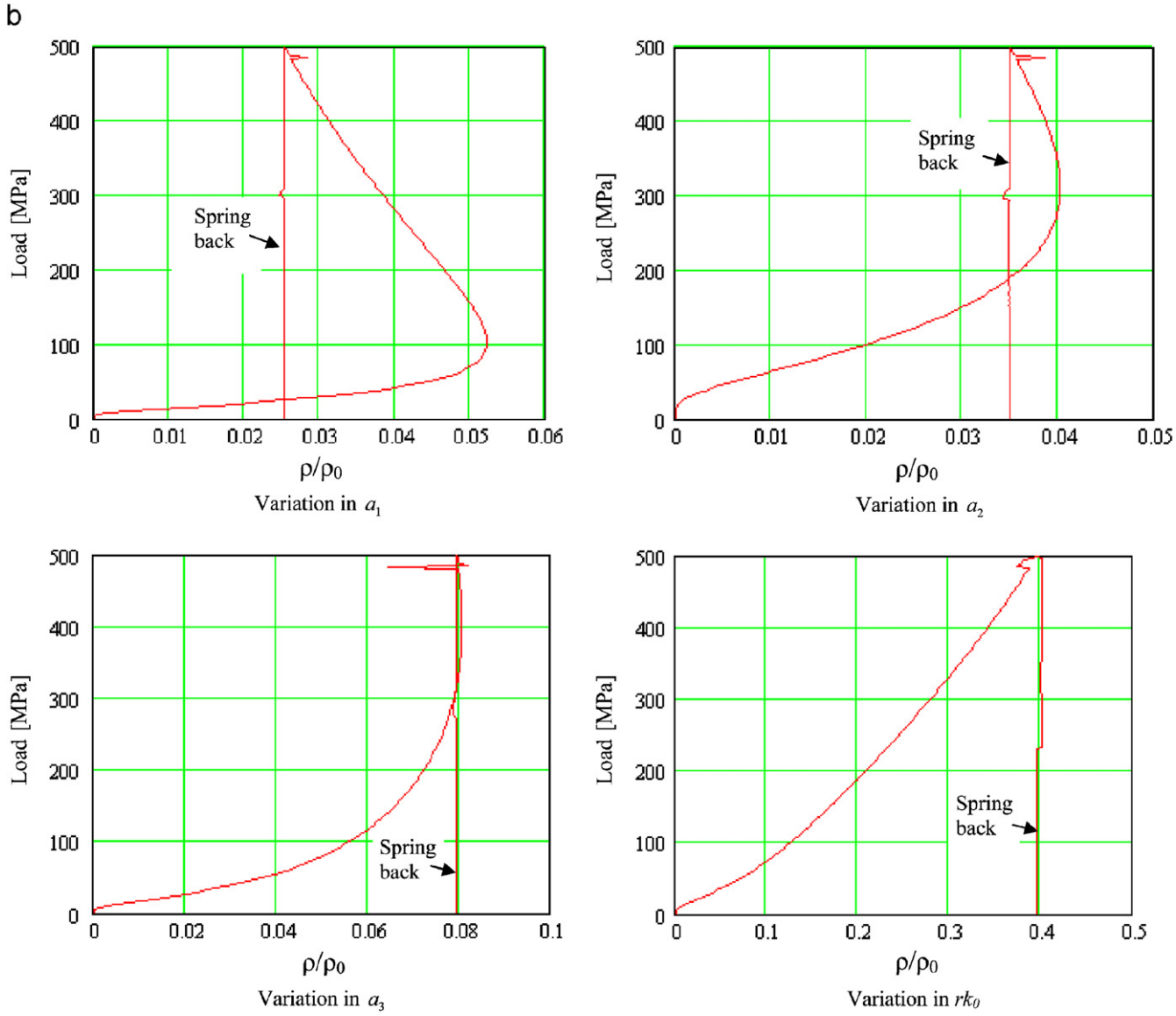

Fig. 13b. Die compaction FE analysis: influence of material parameters on average relative density vs. load response.

constitutive equations. In explicit schemes the time step size has to be small enough to assure stability, i.e., if the time increment is larger than the CFL condition, the increment is said: to have exceeded the *stability limit*. Based on the element-by-element estimate, the stability limit in the linear elastic range defined as

$$\Delta t_{stable} = \frac{L^E}{C_d},$$

where $C_d = \sqrt{\frac{E}{\rho}}$, ρ is density, E the Young modulus and L^E the smallest element size.

In the plastic range, the tangent modulus is smaller then E, and for the CIP process ρ increases as the deformations increase. On the other hand, in extensive deformation, L^E can decrease significantly. Usually the effect of the material properties is more significant then the geometric effect and the stability limit in the linear elastic range is an upper bound for the time step size.

In large distortion cases, it is a common practice to increase ρ artificially in order to increase time step size and reduce computational time. However, the increase in ρ results in artificial inertia forces, which can be significant in high speed process simulation.

Using the values of Λ, μ from Table 1 and $\rho_0 = 8.9 \cdot 10^{-6}\,\mathrm{kg/mm^3}$ for copper, results in $L^E = 2.3 \cdot 10^6 \Delta t_{stable}\,\mathrm{mm/s}$ (at $\rho/\rho_0 = 0.42$ for loose powder at the beginning of the simulation).

The equations of the implicit scheme for the constitutive model evolve in time, hence it is time step size dependent as well. At each time step, the yield function F should converge up to a pre-determined residual value ε. It is evident that as ε is smaller more iteration or smaller time step is required for convergence. Moreover, for the

proposed constitutive model, the convergence space is small, thus small step size is essential to reach convergence at all. The convergence rate depends on the elements shape and deformation gradient value, hence the most effective way would be to adjust the time step to an optimal size at each time step. Unfortunately, this is impossible in Abaqus/Explicit with VUMATs.

In the user subroutine, the residual was set to 10^{-11}, and the maximum number of iterations to 100 at each integration point.

In the computation of the cylindrical sample with a rigid insert, the maximum time step size was set to 10^{-7}, at this value, the subroutine converged in every step for all cases.

In an attempt to reduce computational time, the time step size was increased to $5 \cdot 10^{-7}$. The result was insignificant in the total CPU time, because the number of iterations, at most of the steps, was higher. However, at some steps the maximum number of iteration was reached with a residual of $10^{-9}/10^{-10}$ which is higher than required.

In the explicit scheme, the upper bound for the smallest element size, in that case is: $L^E = 2.3 \cdot 10^6 \cdot 1 \cdot 10^{-7} = 0.23$ mm. This value is relatively large and in order to reduce it the density was increased by a factor of 100, to

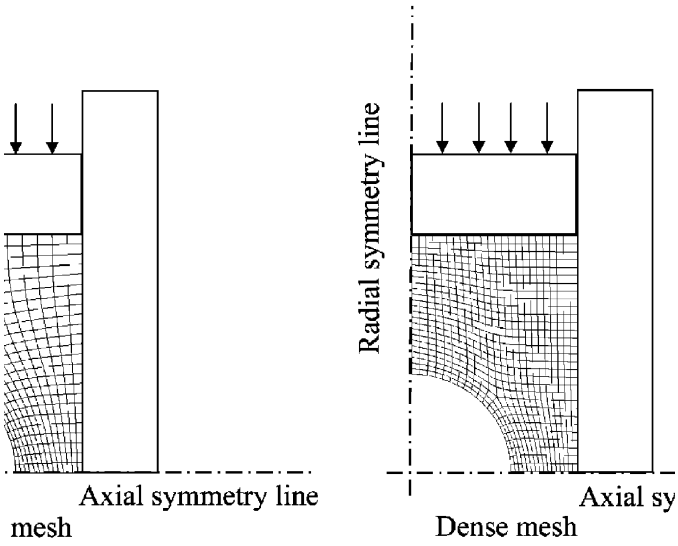

Fig. 16. Four-node quadrilateral FE meshes.

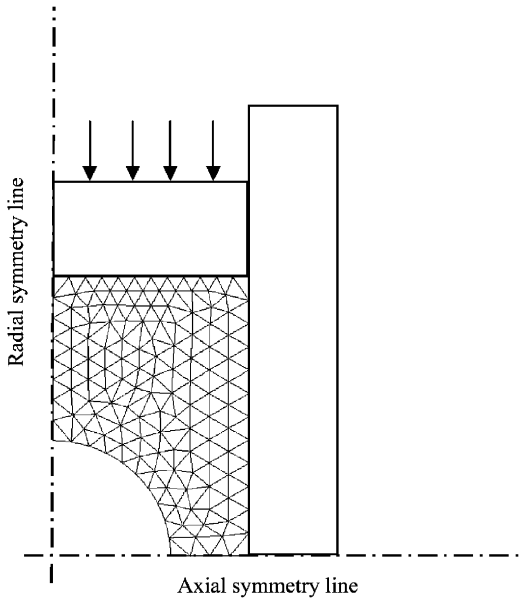

Fig. 17. Triangular FE mesh.

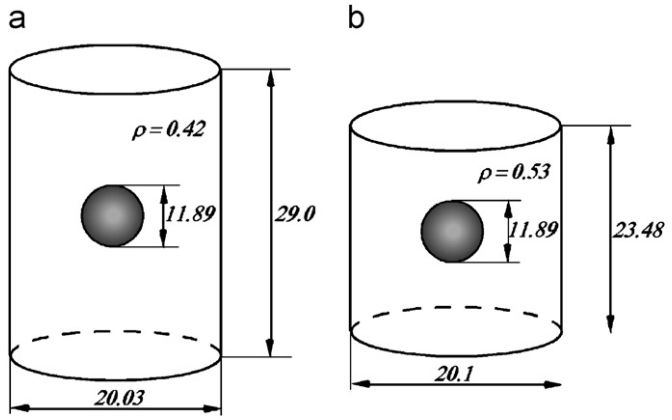

Fig. 14. Cylindrical specimen with a rigid insert. (a) Dimensions (mm) before die compaction, (b) dimensions (mm) before CIP.

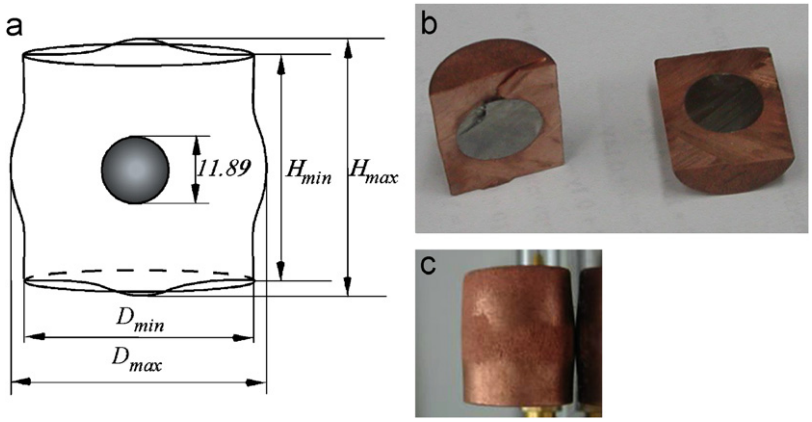

Fig. 15. Final shape of the specimen, after CIP and spring-back (bottom picture shows the specimen after being sliced).

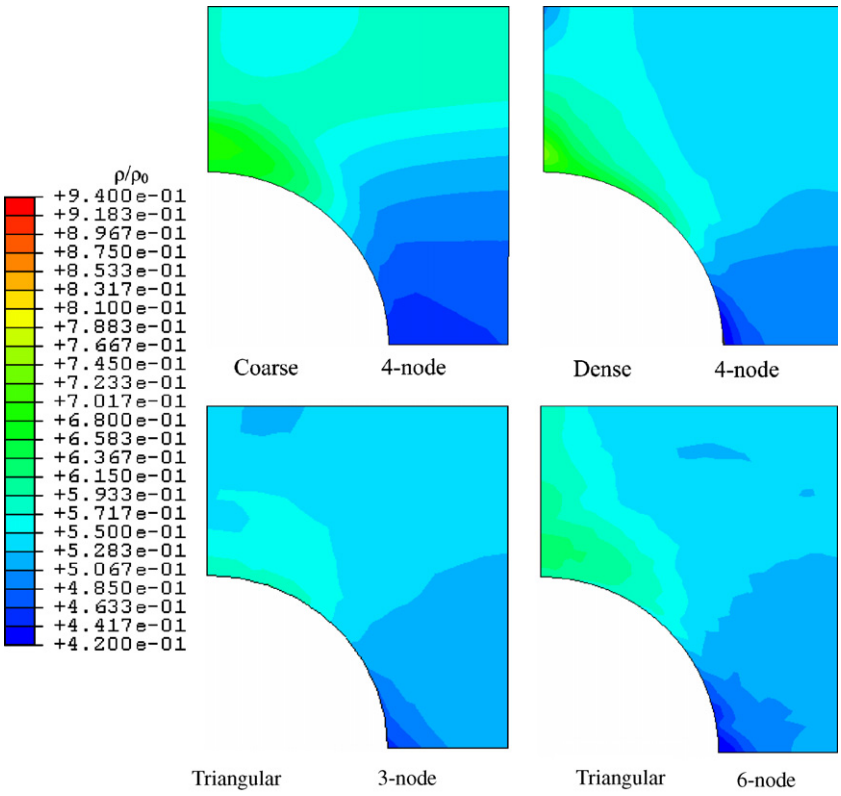

Fig. 18. Relative density distribution after release from die compaction.

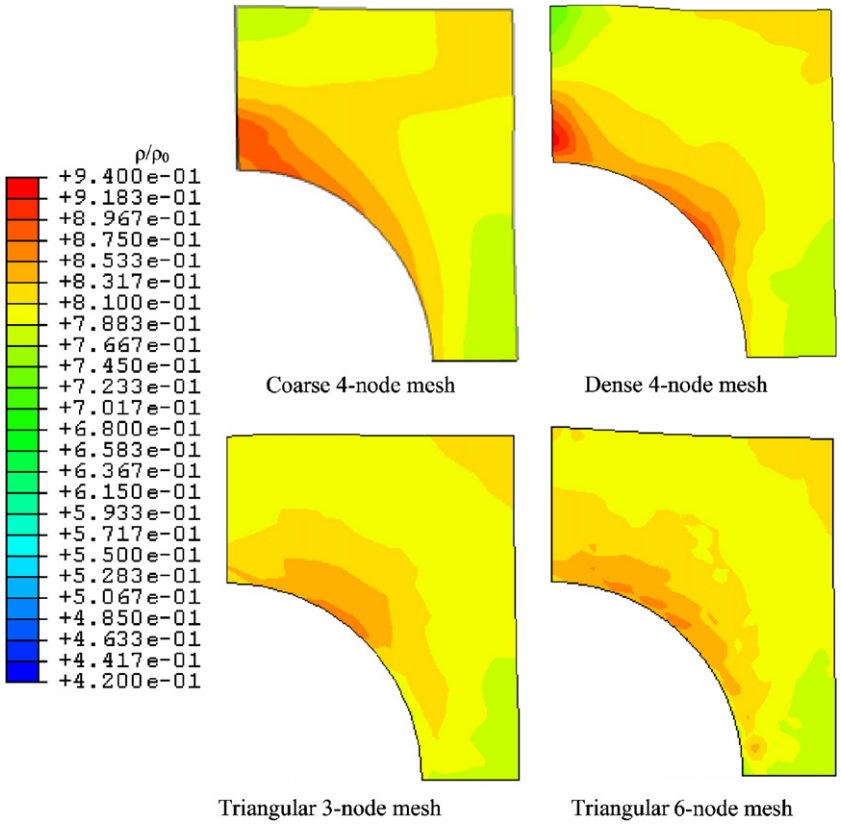

Fig. 19. Relative density distribution at the end of the process (i.e., after CIP unloading).

Table 7
Specimen dimensions (mm) after CIP: FEM analysis and experiments

	H_{min} (mm)	H_{max} (mm)	D_{min} (mm)	D_{max} (mm)	ρ/ρ_0 ave
Experiment	21.09	21.30	17.35	17.61	0.826
(standard deviation)	(0.07)	(0.01)	(0.02)	(0.02)	
Coarse 4-node bilinear	20.95	21.20	17.40	18.05	0.803
(error compared to exp. in %)	(0.67)	(0.47)	(0.30)	(2.56)	(2.78)
Dense 4-node bilinear	20.95	21.45	17.40	17.53	0.828
(error compared to exp. in %)	(0.67)	(0.70)	(0.30)	(0.40)	(0.24)
3-node linear triangular	20.90	21.00	17.60	17.95	0.808
(error compared to exp. in %)	(0.90)	(1.41)	(1.44)	(1.98)	(2.18)
6-node quadratic triangular	20.80	21.45	17.50	17.80	0.816
(error compared to exp. in %)	(1.37)	(0.70)	(0.86)	(1.13)	(1.21)

obtain $L^E \geqslant 0.023$ mm. Since the process is relatively slow, the effect of this value on the solution is insignificant. The code automatically reduces the time step size when smaller values resulted by the computation of the stability limit.

5. Conclusions

The various steps required for a reliable simulation of CIP of metal powders by a commercial explicit FE code have been addressed and demonstrated by comparison of the FE results to experimental observations. The constitutive model for metal powder developed in Ref. [1,11] has been slightly revised herein and implemented as a user subroutine into the commercial FE code Abaqus/explicit.

The required material parameters of the copper powder were identified by die compaction experiments and used to verify the FE implementation. These were subsequently used for the simulation of die compaction followed by CIP of a cylinder with a rigid spherical insert for which experimental observations were available. We have shown that the FE results (dimensions and average relative density) and experimental observations were in very good agreement.

It has to be pointed out that a relatively large computational time was required for each FE analysis on a 2.8 GHz PC. This is due to the explicit algorithm chosen in conjunction with the very small yield surface of the metal powder at low densities. Implementation of the constitutive model into an *implicit FE algorithm* using high order shape functions, although requiring the computation of a tangent stiffness matrix, is expected to provide a dramatic improvement in efficiency of the computations as will be reported in a future work.

Acknowledgments

The authors thank Prof. Moshe Dariel of the Department of Material Engineering at Ben-Gurion University, Beer-Sheva, Israel for helpful discussions, remarks and support.

We also gratefully acknowledge the support of this work by the German-Israeli Foundation for Scientific Research and Development under Grant no. I-700-26.10/2001.

Appendix A. Detailed experimental data of a cylindrical specimen with spherical insert

Specimen	D (mm)	H (mm)	Mass (gm)/(only powder)	Relative density	ha	hb	h upper punch	h bottom punch	H_{max}	H_{min}	D_{max}	D_{min}
Sphere insert of diameter 11.89 mm and mass of 6.8749 m. Die compaction at 52 MPa performed prior to 300 MPa CIP												
A1												
Initial dimens.	20.03	32.66		0.407	59.68	23.59	28.65	21.96				
Dimens. after die compaction	20.1	23.44	38.48 (31.6051)	0.534								
Dimens. after CIP									21.28	21.18	17.58	17.35
A2												
Initial dimens.	20.03	33.21		0.399	61.77	22.05	28.65	21.96				
Dimens. after die compaction	20.1	23.47	38.4692 (31.5943)	0.533								
Dimens. after CIP									21.31	21.13	17.6	17.38
A4												
Initial dimens.	20.03	32.53	38.442 (31.5671)	0.408	61.98	21.16	28.65	21.96				
Dimens. after die compaction	20.1	23.5		0.532								
Dimens. after CIP									21.32	21.05	17.64	17.33
A5												
Initial dimens.	20.03	32.58	38.44(31.5651)	0.408	61.83	21.36	28.65	21.96				
Dimens. after die compaction	20.1	23.5		0.532								
Dimens. after CIP									21.31	21.07	17.62	17.33
A6												
Initial dimens.	20.03	32.5	38.447(31.5721)	0.409	61.85	21.26	28.65	21.96				
Dimens. after die compaction	20.1	23.5		0.532								
Dimens. after CIP									21.3	21.03	17.63	17.35

	D (mm)	H (mm)	Relative density	H_{min} (mm)	H_{max} (mm)	D_{min} (mm)	D_{max} (mm)
Average and standard deviation of experimental data							
Initial dimension							
Average value	20.03	32.696	0.406				
Standard deviation	0	0.294	0.004				
Dimens. after die compaction							
Average value	20.1	23.482	0.533				
Standard deviation	0	0.027	0.001				
Dimens. after CIP							
Average value				21.092	21.304	17.348	17.614
Standard deviation				0.062	0.015	0.020	0.024

References

[1] Bier W, Hartmann S. A finite strain constitutive model for metal powder compaction using a unique and convex single surface yield function. European Journal of Mechanics, Series A/Solids 2006;25: 1009–30.

[2] Khoei A, Lewis RW. Adaptive finite element remeshing in a large deformation analysis of metal powder. International Journal for Numerical Methods in Engineering 1999;45:801–20.

[3] Coube O, Riedel H. Numerical simulation of metal powder die compaction with special consideration of cracking. Powder Metallurgy 2000;43:123–31.

[4] Häggblad H-A. Constitutive models for powder materials. Powder Technology 1991;67:127–36.

[5] Khoei AR, Mofid M, Bakhshiani A. Modelling of powder compaction process using an endochronic model. Journal of Materials Processing Technology 2002;130–131:175–80.

[6] Park S-J, Heung NH, Kyu HO, Lee DN. Model for compaction of metal powders. International Journal of Mechanical Sciences 1999; 41:121–41.

[7] Watson TJ, Wert JA. On the development of constitutive relations for metallic powders. Metallurgical Transactions 1993;24A: 2071–81.

[8] Khoei AR, Azami AR. A single cone-cap plasticity with an isotropic hardening rule for powder materials. International Journal of Mechanical Sciences 2005;47:94–109.

[9] Doremus P, Geindreau C, Martin A, Debove L, Lecot R, Dao M. High pressure triaxial cell for metal powder. Powder Metallurgy 1995;38:284–7.

[10] Chtourou H, Guillot M, Gakwaya A. Modeling ot the metal powder compaction process using the cap model. Part I. Experimental material characterization and validation. International Journal of Solids and Structures 2002;39:1059–75.

[11] Bier W, Dariel MP, Frage N, Hartmann S, Michailov O. Die compaction of copper powder designed for material parameter identification. International Journal of Mechanical Sciences 2007;49:766–77.

[12] Simo J, Pister K. Remarks on rate constitutive equations for finite deformation problems: computational implications. Computer Methods in Applied Mechanics and Engineering 1984;46:201–15.

[13] Mandel J. Plasticité Classique et Viscoplasticité. CISM courses and lectures, vol. 97. Berlin: Springer; 1972.

[14] Carnavas PC. The effect of particle morphology on metal powder compaction. PhD thesis, University of Queensland, Australia; 1996.

[15] Kim KT, Park H. Effect of ceramic ball inclusion on densification of metal powder compact. Material Science and Engineering 2000;A282: 29–37.

[16] Budiansky B. Thermal and thermoelastic properties of isotropic composites. Journal of Composite Materials 1970;4:286–95.

[17] Belytschko T, Liu WK, Moran B. Nonlinear finite elements for continua and structures. Chichester: Wiley; 2000.

[18] Hartmann S, Bier W. High-order time integration applied to metal powder plasticity, International Journal of Plasticity 2008; 24:17–54.